

*Journal of*  
***Mechanics of***  
***Materials and Structures***

**SHOCK-INDUCED DETONATION OF HIGH EXPLOSIVES BY HIGH  
VELOCITY IMPACT**

J. K. Chen, Hsu-Kuang Ching and Firooz A. Allahdadi

***Volume 2, N° 9***

***November 2007***



mathematical sciences publishers



# SHOCK-INDUCED DETONATION OF HIGH EXPLOSIVES BY HIGH VELOCITY IMPACT

J. K. CHEN, HSU-KUANG CHING AND FIROOZ A. ALLAHDAI

We investigate shock-induced detonation of high explosives confined in an open-ended steel cylinder by a normal impact to the cylindrical surface using three-dimensional finite element analysis. Three types of steel projectiles are considered: a cube, a sphere and a square plate. For the encased LX-17 explosive the calculated threshold impact velocities that lead to deflagration and detonation are higher for a sphere than for a cube of the same mass. It is found that detonation of the encased PBXN-110 explosive with the cubical projectile could occur immediately once a full reaction is initiated in the region near the impact site. The threshold detonation velocity is much lower for PBXN-110 than for LX-17. In addition, we discuss the threshold conditions of detonation predicted by different equations of state and failure models for the steel casing and projectile.

## 1. Introduction

When a confined explosive is impacted by a projectile with sufficiently high speed, the energy deposited into the explosive could cause thermal decomposition, and subsequently, initiation of explosion. The two initiation mechanisms are usually shock and shear, depending on the confinement of the explosive and impact conditions. In general, the induced reaction can be classified to be either low-order detonation (deflagration) or high-order detonation (prompt explosion). The latter can massively destroy the assembly of the explosive, whereas the former would merely damage the confinement.

High explosive safety is one of the most important research areas in the field of energetic materials. To meet the safety requirements, a no-reaction event, or at least deflagration, is desired and should be ensured so that no catastrophic accident will occur. Therefore, there is a need for understanding and reliably predicting dynamic response of confined explosives, such as a warhead impacted accidentally by high speed fragments. Although an experimental approach can offer the most accurate results, it is expensive, and sometimes, difficult in implementation due to too many scenarios of warhead design, storage of munitions, and operation deployment. Alternatively, a combined numerical simulation and experiment approach can achieve the goal with a much reduced cost. In this approach firing tests can be conducted with bare or confined explosives impacted by a projectile. Besides predicting the threshold deflagration and detonation conditions, the computer simulation can give detailed information of temporal and spatial impact-to-shock-to-deflagration-to-detonation transition that provides an insight for

---

*Keywords:* explosive detonation, high velocity impact, Lee–Tarver ignition and growth model, Jones–Wilkins–Lee equation of state, Johnson–Cook model, finite element analysis.

The authors would like to thank Mr. Eric Olson of the Air Force Safety Center, Kirtland AFB, New Mexico for his technical and financial support for this project.

understanding the complicated physical processes. Once the numerical solutions are validated with test results, the numerical tool can be used for the safety assessment of real armors.

A great number of numerical studies on detonation of high explosives by projectile impact have been reported so far. Most of them are performed at the coupon level – a projectile impacting onto a flat surface of a bare, front-covered, or totally confined high explosive. Bahl et al. [1981] first used a hydrocode with the nucleation and growth model to compute the threshold impact velocities for bare and slightly covered explosives. This was followed by other hydrocode simulations [Starkenberget al. 1984; Cook et al. 1989; Chou et al. 1991]. Later, the projectile nose shape effects on impact-induced detonation of energetic materials were investigated [James et al. 1991; James et al. 1996; Peugeot et al. 1998; Cook et al. 2001; Shin and Lee 2003a; 2003b; 2003c]. It was found that the threshold detonation velocity is higher for a hemispherical nosed projectile than for a flat-end projectile. For the nose of projectiles with a relatively small cone angle, detonation could occur in a zone of the central axis [Shin and Lee 2003b]. Since all the studies above considered normal impact on the flat surface of bare or confined explosives, the analyses were carried out with either a one-dimensional or two-dimensional axisymmetric model.

On the other hand, only a few numerical investigations on shock initiation of armor are found in the open literature. Allahdadi et al. [1998] utilized the SPH method to simulate sympathetic detonation of an acceptor warhead caused by the impact of fragments resulting from a similar donor warhead. The SPH method was also used by Lattery et al. [2005] to model detonation of a warhead mockup impacted by different fragments. Davison [1997] adopted the AUTODYN hydrocode [Autodyn 2005] to calculate the threshold impact velocity for Octol 70/30 explosive initiation in a 6 inch warhead by a 50 caliber fragment.

In this paper we perform a three-dimensional finite element analysis to model dynamic response of a steel cylinder filled with an LX-17 explosive caused by high velocity projectile impact, using the AUTODYN hydrocode [Autodyn 2005]. The primary goal is to determine the threshold condition that causes detonation of the encased energetic material. Three different shape projectiles are considered: a cube, a sphere, and a square plate. Depending on the projectile investigated, either the threshold detonation velocity or the critical size of the projectile is calculated.

For comparison, shock-induced detonation of an encased PBXN-110 explosive by the cubical projectile impact is also studied. The resulting high rate deformation and perforation of the steel cylinder as well as the shock wave and burn fraction in the explosives are presented and discussed.

It should be pointed out that, due to the complicated physics phenomena involved in the high velocity impact, the computational results presented herein may hinge on the choice of material models. To this end, we also adopt two different equations of state and three failure models in the analysis. The results are compared in terms of threshold detonation.

The paper is organized as follows. Section 2 briefly describes the ignition and growth model for shock detonation of solid explosives, the equation of state for unreacted solid explosives and the reacted gaseous product, and the constitutive models for structural response of the steel casing and projectiles. In Section 3 two different sets of two-dimensional finite element models are studied for generating adequate three-dimensional finite element models for the present numerical analysis. In Section 4 three-dimensional simulations of the shock-to-deflagration-to-detonation transition of the explosives caused by high velocity impact are presented. Conclusions are drawn in Section 5.

## 2. Material models

A mockup consisting of an open-ended steel cylinder filled with an LX-17 or PBXN-110 explosive subjected to steel projectiles is considered in this work. To describe the expansion and detonation of the explosives, the Lee–Tarver ignition and growth model [Lee and Tarver 1980] is employed. As with the forest fire model [Forest 1978], the Lee–Tarver model is based on the assumption that ignition starts at local hot spots and grows outward from these sites. The reaction rate for the conversion of unreacted explosive to gaseous product is given by

$$\frac{\partial F}{\partial t} = I(1 - F)^b \left( \frac{\rho}{\rho_0} - 1 \right)^x + G(1 - F)^c F^d p^y, \quad (1)$$

where  $F$  is the reaction ratio,  $p$  is the pressure,  $\rho_0$  and  $\rho$  are the initial and current densities, respectively, and  $I, b, x, G, c, d,$  and  $y$  are constants.

Both the unreacted solid and the reacted gaseous product of LX-17 explosive are characterized with the Jones–Wilkins–Lee (JWL) equation of state [Lee et al. 1968]. The pressure in either phase is defined in terms of volume and internal energy as

$$p = A \left( 1 - \frac{\omega}{R_1 V} \right) e^{-R_1 V} + B \left( 1 - \frac{\omega}{R_2 V} \right) e^{-R_2 V} + \frac{\omega e}{V}, \quad (2)$$

where  $V = \rho/\rho_0$  is the relative volume,  $e$  is the internal energy, and  $A, B, R_1, R_2,$  and  $\omega$  are constants. The values of the above constants for a reacted gaseous product are different from those for the unreacted solid explosive.

For the PBXN-110 explosive the JWL equation (2) is employed for the reacted gaseous product while the Mie–Gruneisen form of equation of state is used for the unreacted solid, which is given by

$$p = p_H + \Gamma \rho (e - e_H), \quad p_H = \frac{\rho_0 c_0 \mu (1 + \mu)}{[1 - (s - 1)\mu]^2}, \quad e_H = \frac{p_H}{2\rho_0} \left( \frac{\mu}{1 + \mu} \right), \quad \rho \Gamma = \rho_0 \Gamma_0, \quad \mu = \frac{\rho}{\rho_0} - 1, \quad (3)$$

where  $\Gamma_0, c_0,$  and  $s$  are constants.

Both the cylinder and all the projectiles are modeled as 4340 steel. With the high impact pressure and the blast force resulting from explosive detonation, the shock equation of state for most metals [Meyers 1994] and the Johnson–Cook plasticity model [Johnson and Cook 1983] that accounts for the effects of strain hardening, strain-rate hardening, and thermal softening are adopted to describe the dynamic response of the steel. They are expressed as

$$U = c_0 + s u_p, \quad Y = [A_0 + B_0 \varepsilon_p^n] [1 + C_0 \log \dot{\varepsilon}_p^*] [1 - T^*], \quad (4)$$

where  $U$  and  $u_p$  are the shock and particle velocities, respectively,  $Y$  is the yield stress,  $\varepsilon_p$  is the effective plastic strain,  $\varepsilon_p^* = \dot{\varepsilon}_p / \dot{\varepsilon}_p^0$  is the normalized effective plastic strain rate,  $T^* = (T - T_{\text{room}}) / (T_{\text{melt}} - T_{\text{room}})$  is the homologous temperature, and  $A_0, B_0, C_0, m,$  and  $n$  are constants.

The values of the material parameters in Equations (1)–(3) for the LX-17 and PBXN-110 explosives and in Equation (4) for the 4340 steel used in the present analysis are given in Tables 1 and 2, respectively.

Material Constants	LX-17	PBXN-110
$\rho_0$ (g/cm <sup>3</sup> )	1.905	1.67
$I$ ( $\mu$ s)	50	33
$b$	0.222	0.667
$x$	4.0	4.0
$G$	500	600
$c$	0.222	0.667
$d$	0.667	0.222
$y$	3	3
$A_r$ (Mbar)	6.5467	4.69924
$B_r$ (Mbar)	0.071236	0.00106
$R_{1,r}$	4.45	3.86
$R_{2,r}$	1.2	1.0
$\omega_r$	0.35	0.40
$A_u$ (Mbar)	778.09999	
$B_u$ (Mbar)	-0.05031	
$R_{1,u}$	11.3	
$R_{2,u}$	1.13	
$\omega_u$	0.8939	
$\Gamma_0$		0.8
$c_0$		0.199
$s$		3.05

**Table 1.** Material constants in Equations (1)–(3) for the Lee–Tarver ignition and growth model, JWL equation and shock EOS for LX-17 [Tarver and Hallquist 1981] and PBXN-110 [Miller 1996] explosives. Subscripts  $u$  and  $r$  denote the unreacted explosive and reacted product, respectively.

Shock EOS		JC plasticity model		JC damage model	
$\rho_0$ (g/cm <sup>3</sup> )	7.83	$A_0$ (Mbar)	0.0051	$D_1$	0.05
$\Gamma_0$	2.17	$B_0$	0.26	$D_2$	3.44
$c_0$	0.4569	$C_0$	0.014	$D_3$	-2.12
$s$	1.49	$m$	1.03	$D_4$	0.002
		$T_{\text{melt}}$ (°K)	1793	$D_5$	0.61

**Table 2.** For 4340 steel, values of material constants used in Equation (4) for the shock EOS [Meyers 1994] and the Johnson–Cook plasticity model [Johnson and Cook 1983], and in Equation (6) for the Johnson–Cook damage model [Johnson and Cook 1985]. Shear modulus is 0.818 mbar.

### 3. Computational modeling

A schematic sketch for the mockup impacted by a cubical projectile is depicted in Figure 1. The open-ended steel cylinder is 10 cm long and 0.9525 cm thick; the encased explosive is 6.6675 cm in radius. The projectile is assumed to strike normally on the cylindrical surface at time  $t = 0$  and directly toward the centroid of the mockup. For convenience, we use a rectangular Cartesian coordinate system with origin located at the centroid of the mockup and the  $z$ -axis parallel to the axial axis. Thus, the central line of the projectile trajectory is along the positive  $x$ -axis.

The shock-induced detonation of the confined explosives by the steel projectile impact is simulated with the AUTODYN finite element processor. To ensure the accuracy of the three-dimensional numerical solutions, analyses with two sets of plane strain finite element models, namely, two-dimensional case I and two-dimensional case II, are first performed for the convergence study. The former is selected for the circular cross-section of the mockup at  $z = 0$ , and the latter is selected for the rectangular cross-section perpendicular to the  $y$ -axis at  $y = 0$ . We chose the two cross-sections for the convergence study because the most severe deformation is present in these areas. Due to the symmetry of the structural geometry and the impact loading, only half of each cross-section is analyzed. Each finite element model includes the corresponding two-dimensional portion of the cubical projectile of 7 g. For plotting the time history of the desired variables, points  $A$  and  $B$  in the explosive are assigned at  $(-6.2, 0, 0)$  cm and  $(-6.6675, 0, 0)$  cm, respectively. Point  $B$  is the intersection point between the central line of the projectile trajectory and the cylindrical interface between the casing and explosive.

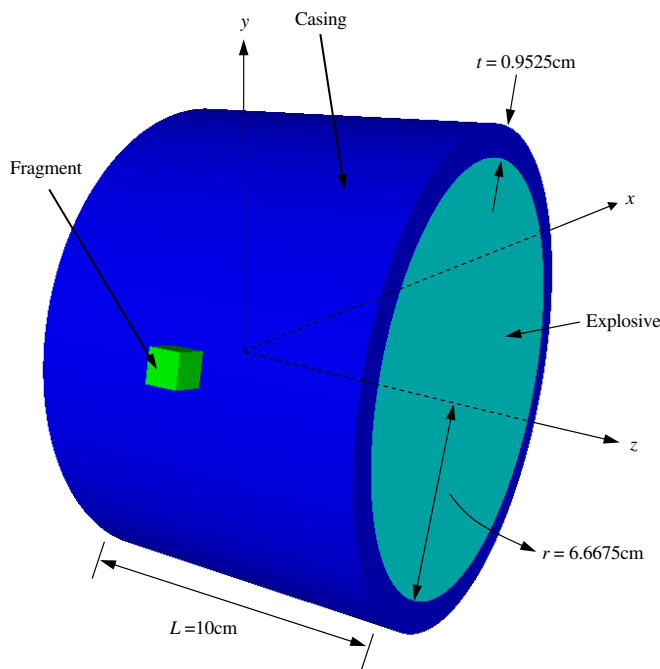


**Figure 1.** Schematic sketch of a mockup impacted by a single projectile.

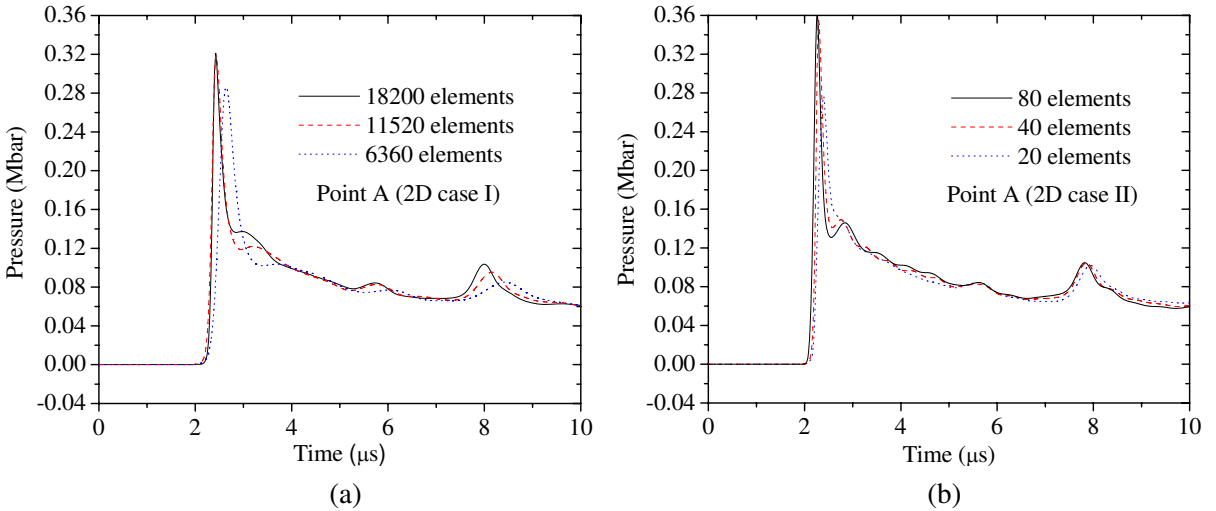


**Figure 2.** Time histories of the shock pressure at point A computed with different mesh densities for (a) two-dimensional case I and (b) two-dimensional case II; the impact velocity is 3.0 km/s.

Figure 2(a) shows the time history of shock pressure  $p$  at point A caused by the 7 g cubical projectile impact at a speed of 3.0 km/s, calculated with three different meshes for the two-dimensional case I. It appears that the results obtained with the finite element models of 11,520 and 18,200 elements are close to each other, thereby indicating that the mesh of 11,520 elements is sufficient to discretize the circular cross-section. For the two-dimensional case II, the number and size of the elements along the  $x$ -axis are identical to those in the mesh of 11,520 elements tested in the two-dimensional case I. The nodes along the  $z$ -direction are nonequally spaced with a smaller spacing for those located near the  $x$ -axis. Comparing the results in Figure 2(b) shows no appreciable difference in pressure at point A between the two models in which 40 elements and 80 elements are meshed in the axial direction. Therefore, the mesh with the 40 elements in the  $z$ -direction is adequate for the discretization of the model.

The mesh of 11,520 elements for the circular cross-section at  $z = 0$  and the one with 40 elements in the  $z$ -direction for the rectangular cross-section perpendicular to the  $y$ -axis at  $y = 0$  are the two bases in constructing the adequate three-dimensional finite element models. Figure 3 depicts a three-dimensional model generated for a quadrant of the mockup and the cubical projectile, in which a total of 461,824 elements are employed. It is used in the simulations of the mockup impacted by the cubical projectile in Sections 4.1 and 4.4. When the other shape projectiles are studied, only the projectile portion of the finite element model is modified.

During the calculation, some of the elements may become grossly distorted. A so-called erosion criterion is adopted to remove such elements from the analysis. This criterion considers an element to have failed if a predefined strain such as the instantaneous geometrical strain or the effective plastic strain exceeds a specified limit. In this study an element is removed when the instantaneous effective

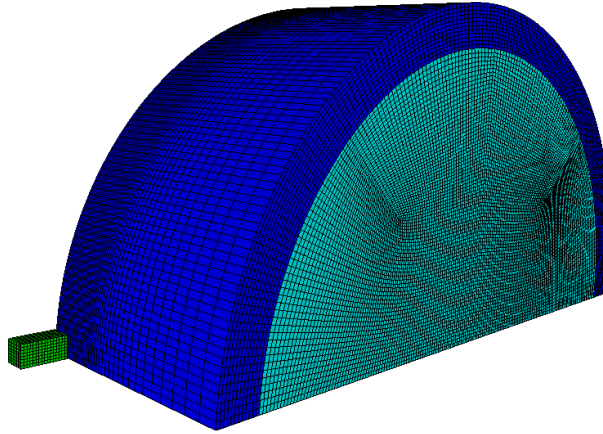


**Figure 3.** Three-dimensional finite element model for mockup impacted by a 0.96 cm cubical steel projectile.

geometrical strain  $\bar{\epsilon}_{\text{eff}}$  250%.  $\bar{\epsilon}_{\text{eff}}$  is defined as the integral of the incremental effective geometric strain

$$\bar{\epsilon}_{\text{eff}} = \int \Delta \bar{\epsilon}_{\text{eff}} dt, \quad \Delta \bar{\epsilon}_{\text{eff}} = \Delta t \sqrt{\frac{2}{3} (\dot{\epsilon}_{xx}^2 + \dot{\epsilon}_{yy}^2 + \dot{\epsilon}_{zz}^2 + \dot{\epsilon}_{xy}^2 + \dot{\epsilon}_{yz}^2 + \dot{\epsilon}_{zx}^2)},$$

where  $\dot{\epsilon}_{ij}$  are the strain rates and  $\Delta t$  the time increment.

#### 4. Results and discussion

The shock-induced detonation of LX-17 explosive studied in Sections 4.1–4.3 is for the impact by the three different shapes of projectile, and the PBXN-110 explosive studied in Section 4.4 is for the impact by the cubical projectile. Depending on the projectile investigated, either the threshold detonation velocity or the critical size of the projectile is determined.

**4.1. Impact by a 7 g cubical steel projectile.** This case is to determine the threshold impact velocities that leads to deflagration and detonation of the encased LX-17 explosive by the 7 g cubical steel projectile of 0.96 cm on each side. To do so, successive numerical analyses are performed by varying impact speeds.

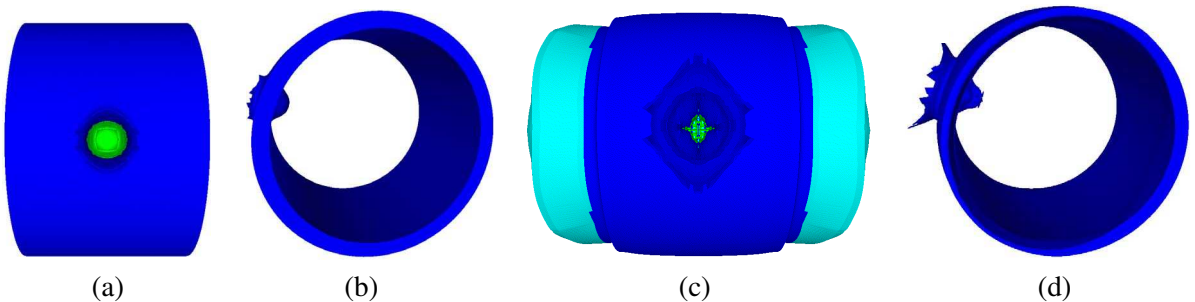


**Figure 4.** Mockup, cubical fragment and deformed outer casing at  $t = 20 \mu\text{s}$ ; (a,b):  $V_p = 2.3 \text{ km/s}$  and (c,d):  $V_p = 4.6 \text{ km/s}$ .

First, dynamic behaviors of the steel casing and the encased explosive are investigated for two simulated impact velocities,  $V_p = 2.3$  km/s and 4.6 km/s. Figure 4 shows the configurations of the mockup and projectile as well as the deformation of the casing at  $t = 20 \mu\text{s}$ . Apparently, the structural and explosive responses respectively are quite different between the two impact speeds. The rapid expansion of the explosive outward from both ends of the cylinder shown in Figure 4(c) for the impact at  $V_p = 4.6$  km/s indicates that the explosive is undergoing a violent detonation. On the other hand, for the lower impact velocity of 2.3 km/s there is no discernible expansion of the explosive (Figure 4(a)) but a crater-like damage in the steel casing (Figure 4(b)). The overall damage to the casing is not so severe as that caused by the impact speed of 4.6 km/s, for which not only the casing is perforated, but the outer rim of the crater buckles as well; see Figure 4(d). Accordingly, it can be deduced that the threshold detonation speed of the encased LX-17 explosive must lie in between 2.3 km/s and 4.6 km/s.

Figure 5(a) compares the time histories of burn fraction  $\alpha$  at point A for four impact speeds ranging from 2.3 km/s to 4.6 km/s. For the speed of 2.3 km/s the burn fraction is quite small, only about 2.5%. This confirms the statement made previously that the explosive is not fully ignited yet. As the speed increases to 3.8 km/s, the explosive at point A accounts for about 92% of burn fraction. It then fully reacts ( $\alpha = 1$ ) at 3.9 km/s. This suggests that the speed of the 7 g cubical steel projectile be at least about 3.9 km/s for full ignition. The corresponding shock pressures at point A are given in Figure 5(b). For all four impact speeds a sharp pressure spike is present while the shock wave is passing through point A. As expected, the strength of the shock wave increases as the impact velocity increases. It is worth noting that the maximum shock pressure induced by the impact at 3.9 km/s is 0.325 Mbar, which is the minimum pressure needed for the LX-17 explosive to fully react. The fact that the peak pressure at point B shown in Figure 5(b) is higher than 0.325 Mbar reveals that for the impact velocity 4.6 km/s the detonation

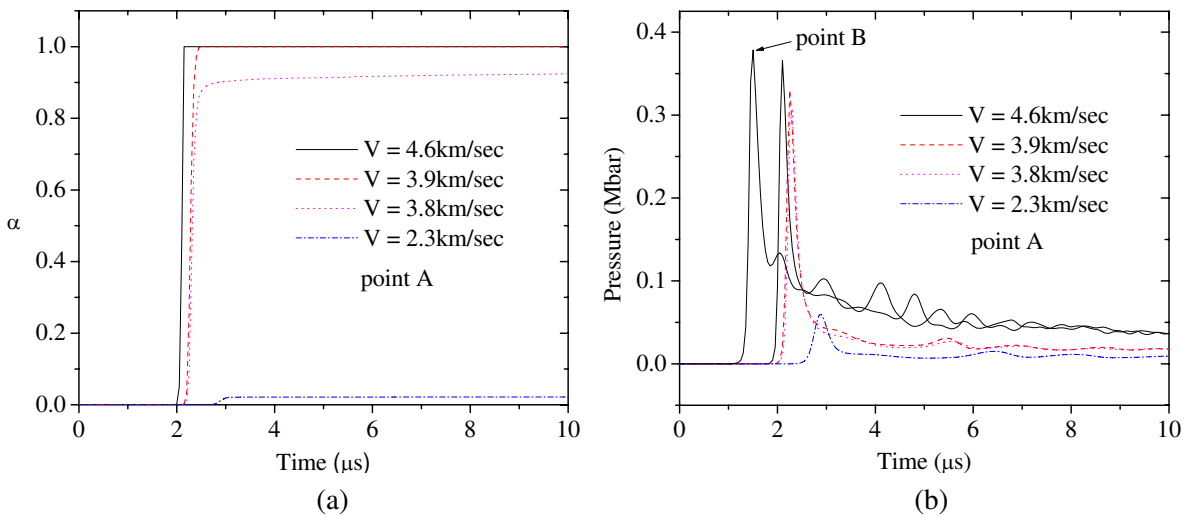


**Figure 5.** Time histories of (a) burn fraction and (b) shock pressure at point A  $(-6.2, 0, 0)$  cm for four impact velocities; the shock pressure at point B  $(-6.6675, 0, 0)$  cm for  $V_p = 4.6$  km/s is also included in (b).

directly results from the pressure transmitted from the impact. Recall that point  $B$  is the intersection point between the central line of the projectile trajectory and the cylindrical interface between the steel casing and explosive.

Although the critical impact velocity for full reaction at a point such as, for example,  $A$  has been identified, initiation of explosion may not be claimed unless the succeeding pressure is strong enough to sustain the fast growth of detonation. During the shock wave propagation in a reactive material two processes are competing with each other for the shock strength. One is the rarefaction of the stress wave that is transmitted from the impact, and the other is the buildup of gas pressure from partial and/or full reaction of the solid explosive. If the latter prevails over the former, the shock wave will be amplified and, in turn, will lead to detonation after it travels a certain distance in the explosive. Otherwise, the shock wave will become weaker and weaker, and eventually will lose its ability to react with the explosive charge.

Continuing our numerical search for high-order detonation Figure 6 shows shock wave propagation in the circular cross-section at  $z = 0$  for the impact speed of 4.4 km/s at  $t = 3 \mu\text{s}$ ,  $5 \mu\text{s}$ ,  $10 \mu\text{s}$ , and  $20 \mu\text{s}$ . It is clearly seen that the shock wave continues rarefying as it propagates outward radially from the impact region. A different shock wave evolution resulting from for the impact speed 4.5 km/s is shown in Figure 7. Early on the shock waves generated by the two impact speeds are similar and the peak pressures are also close. For example, at  $t = 2 \mu\text{s}$  the peak pressures are 0.364 Mbar caused by the impact at 4.4 km/s and 0.365 Mbar by 4.5 km/s. Similar results are seen in Figures 6(a) and 7(a) for  $t = 3 \mu\text{s}$ . At later times, however, the shock wave induced by the impact speed of 4.5 km/s not only is intensified continuously, but its profile changes as well; see the rest of Figure 7. The strengthening of the shock wave implies that the buildup of the gas pressure is the dominating mechanism for this case. As indicated in Figure 7(c), the shock wave front hits the interface between the explosive and the casing at about  $12 \mu\text{s}$ .

Afterwards, parts of the shock wave are reflected from both the top and low interfaces and then travel back to the impact side along the cylindrical interface, while the rest part of the wave continues moving toward the other side at  $x = 6.6675 \text{ cm}$ . The two shock waves that travel back to the impact side interfere with each other after they reflect from the interface near the impact site. As a result of the constructive interference, the strength of the superposed shock wave in the vicinity of the  $x$ -axis increases; see Figures 7(e) and (f).

The burn fraction  $\alpha$  is an indicator for explosive detonation, with which an explosive is said to be fully reacted when  $\alpha = 1$ , inert when  $\alpha = 0$ , and partially reacted when  $0 < \alpha < 1$ . Figure 8 displays the burn fraction distribution over the circular cross-section at  $z = 0$  for the two impact speeds 4.4 km/s and 4.5 km/s at four different instants,  $t = 5 \mu\text{s}$ ,  $10 \mu\text{s}$ ,  $15 \mu\text{s}$  and  $20 \mu\text{s}$ . At  $t = 2 \mu\text{s}$  the maximum burn fraction is 0.15 for the impact speed of 4.4 km/s and 0.23 for 4.5 km/s, occurring near point  $B$ . For both speeds the onset of the full reaction starts sometime in between  $2 \mu\text{s}$  and  $3 \mu\text{s}$ . It is clearly visible in Figures 8(a)–(d) for the impact speed of 4.4 km/s that the explosive only deflagrates since the reaction does not grow, but is instead confined to a small volume. For the impact speed of 4.5 km/s, however, a full reaction rapidly grows and spreads as illustrated by the evolved contours of the burn fraction shown in Figures 8(e)–(h). The entire cross-section detonates at about  $t = 20 \mu\text{s}$ , when the reflected shock waves superpose at the  $x$ -axis. The average detonation rate in the  $x$ -direction estimated from Figures 8(f) and (g) for the time interval  $t = 10$ – $15 \mu\text{s}$ , for instance, is about  $0.752 \text{ cm}/\mu\text{s}$ .

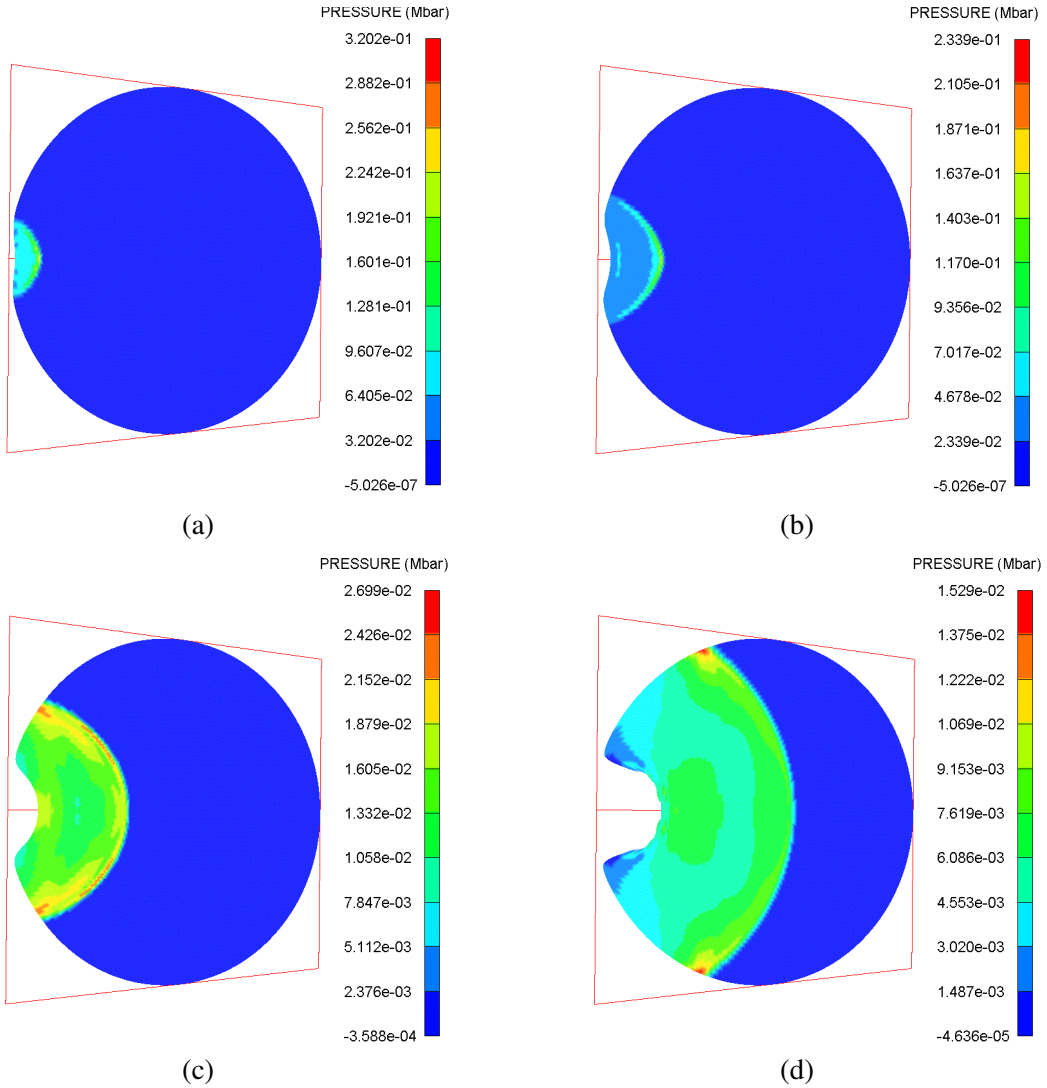


**Figure 6.** Shock wave propagation in the explosive circular cross-section at  $z = 0$  for impact speed of 4.4 km/s for  $t =$  (a)  $3 \mu\text{s}$ , (b)  $5 \mu\text{s}$ , (c)  $10 \mu\text{s}$ , (d)  $20 \mu\text{s}$ .

The results above indicate that for the open-ended steel cylinder of 10 cm in length and 0.9525 cm in thickness filled with the LX-17 explosive of 6.6675 cm in radius under a normal impact to the cylindrical surface by a 7 g cubical steel projectile, the simulated threshold impact velocity is 3.9 km/s for deflagration and 4.5 km/s for detonation.

**4.2. Impact by a spherical steel projectile of 7 g.** For comparison we discuss the detonation of the same mockup induced by a spherical projectile of the same mass as the cubical one, namely, 7 g. The calculated threshold velocity is about 4.5 km/s for deflagration and about 4.8 km/s for detonation. Both threshold velocities are higher than those found for the cubical projectile. The resulting shock waves are similar to those in Figure 7 for the cubical projectile; we omit them for brevity. The higher threshold detonation

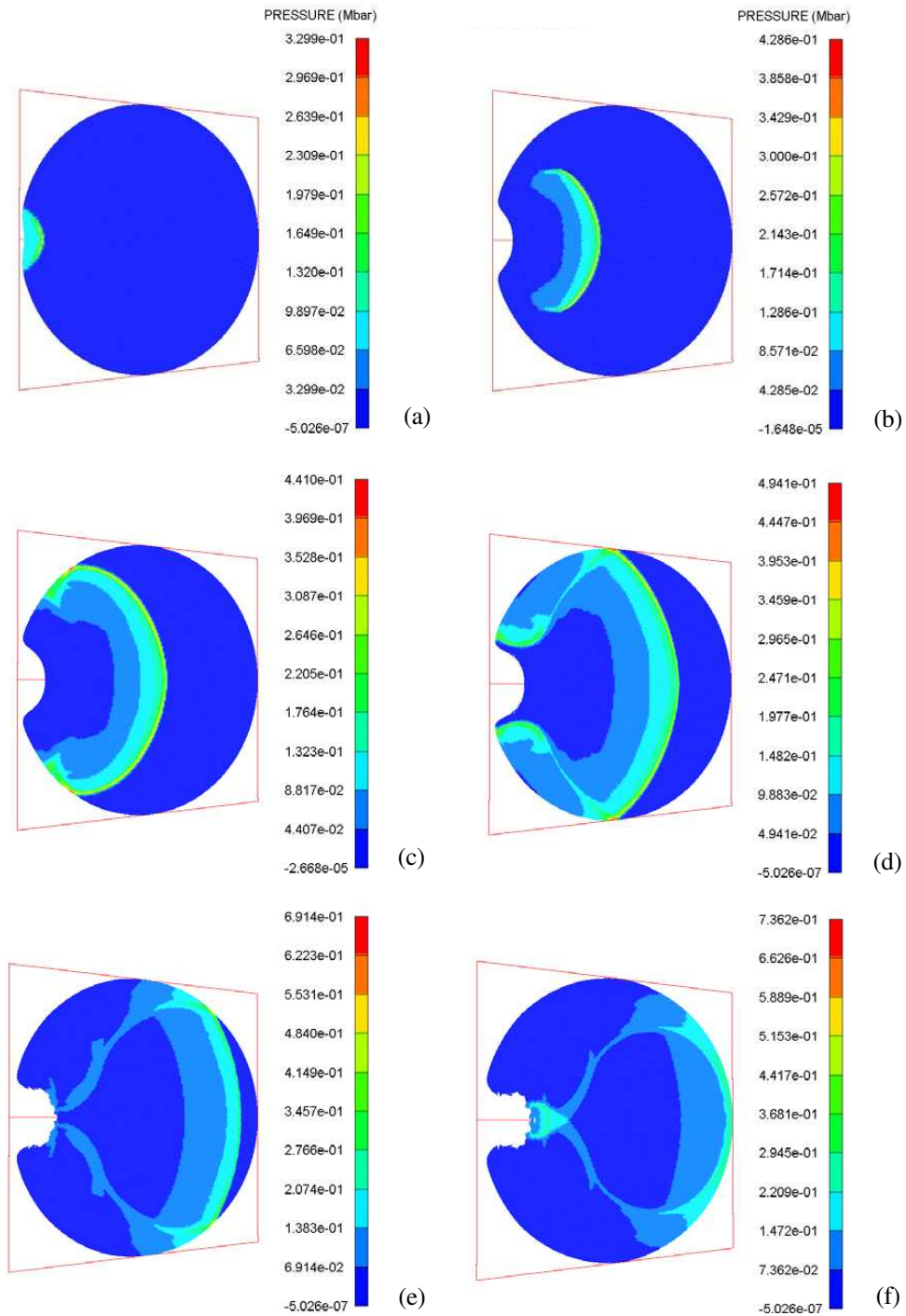


**Figure 7.** Shock wave propagation in the explosive circular cross-section at  $z = 0$  for impact speed 4.5 km/s for  $t =$  (a)  $3 \mu\text{s}$ , (b)  $9 \mu\text{s}$ , (c)  $12 \mu\text{s}$ , (d)  $15 \mu\text{s}$ , (e)  $18 \mu\text{s}$ , (f)  $20 \mu\text{s}$ .

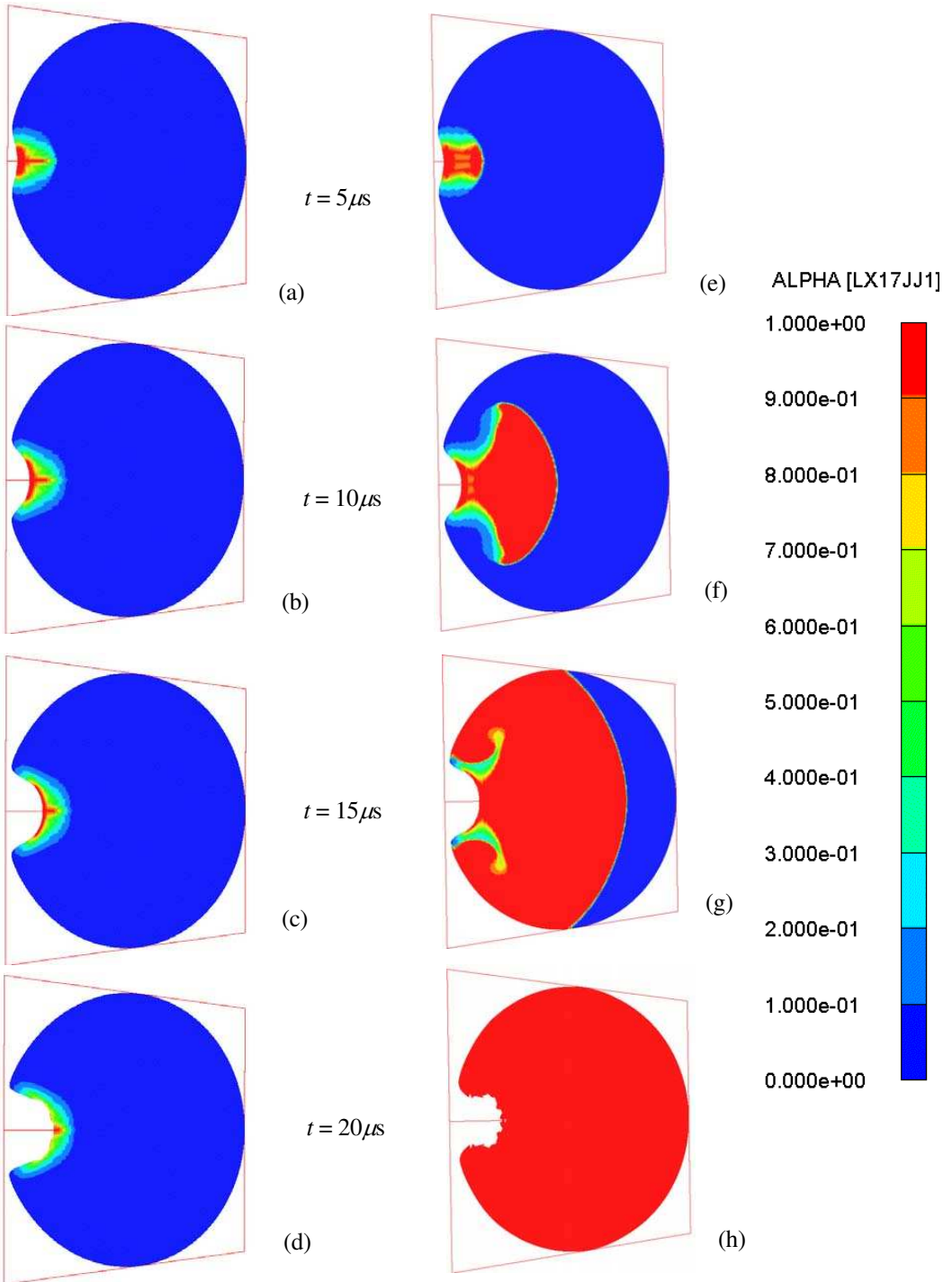


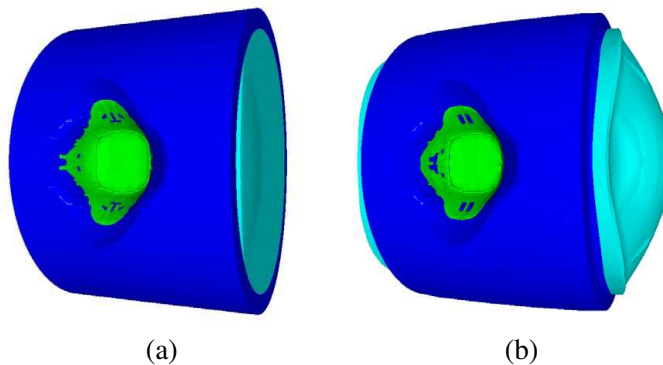
**Figure 8.** Burn fraction of the explosive in the circular cross-section at  $z = 0$  at  $t = 5 \mu s, 10 \mu s, 15 \mu s$  and  $20 \mu s$ ; (a-d):  $V_p = 4.4 \text{ km/s}$  and (e-h):  $V_p = 4.5 \text{ km/s}$ .

velocity for the spherical projectile found here is consistent with those found for the projectiles impacting on a flat surface of a bare, front-covered, or totally confined high explosive [Hull et al. 2002].

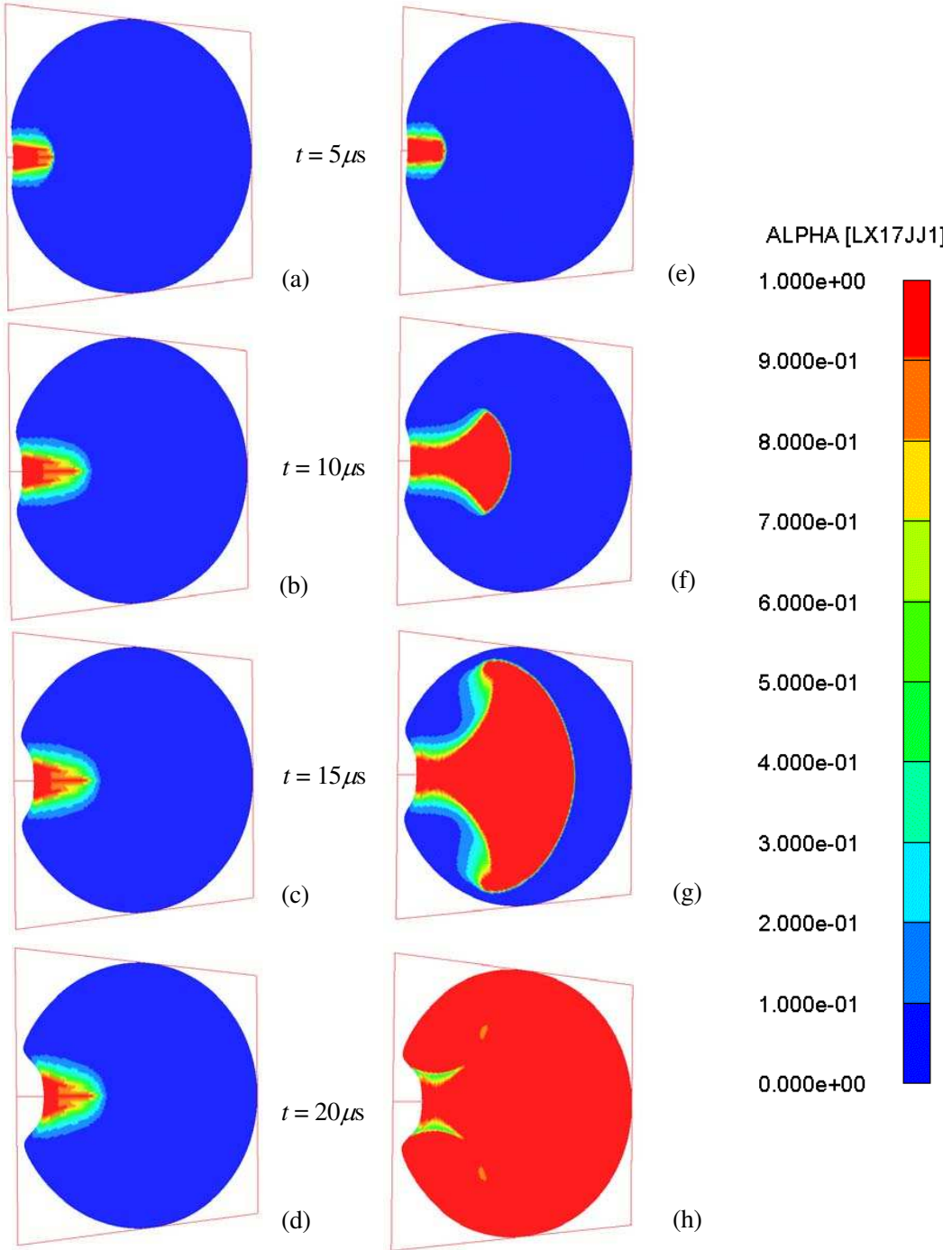
**4.3. Impact by a square plate at constant velocity of 2.3 km/s.** Here we study the detonation of the encased LX-17 explosive caused by a square plate projectile of thickness 0.96 cm, same as the cubical projectile. The impact speed is kept constant at 2.3 km/s. The aim is to determine the threshold detonation in-plane dimensions of the plate. Successive numerical simulations are performed with the three-dimensional finite element models modified according to the change of the in-plane dimensions of the square plate.

Figure 9 shows the deformed configurations of the mockup at  $t = 20 \mu\text{s}$  simulated for the impact by two projectiles with the in-plane square dimensions of 1.73 cm and 1.74 cm, respectively. Prompt detonation caused by the latter is evidenced by the significant, rapid expansion of the explosive in Figure 9(b), while the former may only cause deflagration as per the inconsequential expansion indicated in Figure 9(a). The burn fractions in the circular cross-section of the explosive at  $z = 0$  shown in Figure 10 further verify the above conjecture. The widths of the crater in and the regions of the reaction of the explosive are slightly larger than those found in the case of the cubical projectile due to the larger in-plane size, but otherwise the evolutions of the explosive reaction are similar. The lower threshold detonation velocity for a wider projectile of the same thickness as the cubic projectile calculated here is as expected.

**4.4. PBXN-110 explosive impacted by a 7 g cubical steel projectile.** Figure 11 depicts the burn fractions in the encased PBXN-110 explosive at  $t = 20 \mu\text{s}$  caused by the 7 g cubical steel projectile for the impact velocities of 2.9 km/s and 3.0 km/s. The explosive does not fully react when impacted by the cube at 2.9 km/s, since the maximum burn fraction is 0.927. It is interesting to note, however, that as we increase the impact speed by only 0.1 km/s to 3.0 km/s, violent detonation now occurs. Besides the lower threshold detonation velocity (3.0 km/s here versus 4.5 km/s for the LX-17 explosive), the direct shock-to-detonation transition found here is different than the shock-to-deflagration-to-detonation transition found for the LX-17 explosive in Section 4.1.



**Figure 9.** Mockup and projectile at  $t = 20 \mu\text{s}$  resulting from impact of two flat projectiles with  $V_p = 2.3 \text{ km/s}$ ; (a)  $1.73 \text{ cm} \times 1.73 \text{ cm} \times 0.96 \text{ cm}$  and (b)  $1.74 \text{ cm} \times 1.74 \text{ cm} \times 0.96 \text{ cm}$ .



**Figure 10.** Burn fraction of the explosive in the circular cross-section at  $z = 0$  caused by two flat projectiles at  $V_p = 2.3 \text{ km/s}$  for  $t = 5 \mu s, 10 \mu s, 15 \mu s$  and  $20 \mu s$ ; (a-d):  $1.73 \text{ cm} \times 1.73 \text{ cm} \times 0.96 \text{ cm}$  and (e-h):  $1.74 \text{ cm} \times 1.74 \text{ cm} \times 0.96 \text{ cm}$ .

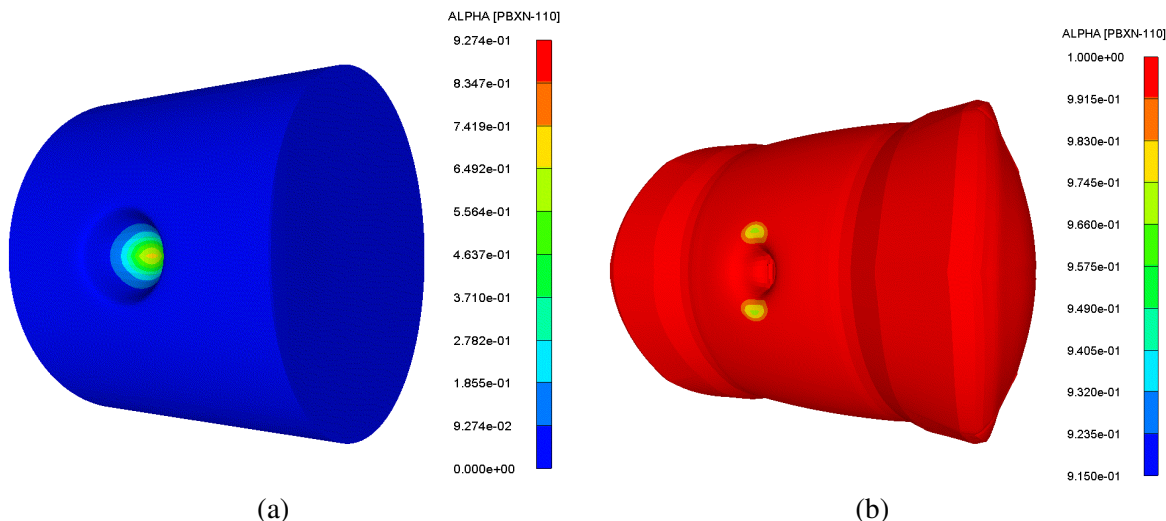


**Figure 11.** Burn fraction of the encased PBXN-110 explosive at  $t = 20 \mu\text{s}$  for (a)  $V_p = 2.9 \text{ km/s}$  and (b)  $V_p = 3.0 \text{ km/s}$ .

Figure 12 shows the shock wave propagation in the circular cross-section at  $z = 0$  for  $V_p = 2.9 \text{ km/s}$  and  $3.0 \text{ km/s}$  at  $t = 5 \mu\text{s}$ ,  $8 \mu\text{s}$ ,  $10 \mu\text{s}$  and  $15 \mu\text{s}$ . Clearly, the shock wave is getting stronger with time for the case of  $3.0 \text{ km/s}$ . This is again attributed to the rapid pressure buildup from the explosive reaction. Note that, except for early time, the wave profiles in Figures 12(e)–(h) are different from those in Figure 7. The shock wave front hits the interface between the explosive and the casing much earlier at about  $7 \mu\text{s}$  compared to  $12 \mu\text{s}$  as seen in Figure 7(c). It then takes about  $3 \mu\text{s}$  for the two reflected waves to superpose in the vicinity of the central axis of the projectile trajectory; compare this to  $8 \mu\text{s}$  shown in Figure 7(f).

The burn fraction in the circular cross-section at  $z = 0$  is presented in Figure 13. A full reaction of the explosive takes place in the region near the impact site at about  $t = 5 \mu\text{s}$  where the peak pressure is  $0.369 \text{ Mbar}$ . The estimated average detonation rate in the  $x$ -direction is  $0.830 \text{ cm}/\mu\text{s}$  for  $t = 6\text{--}8 \mu\text{s}$ ,  $0.850 \text{ cm}/\mu\text{s}$  for  $t = 8\text{--}10 \mu\text{s}$ , and  $0.862 \text{ cm}/\mu\text{s}$  for  $t = 10\text{--}15 \mu\text{s}$ . Comparison of the results in Figure 13 and Figures 8(e)–(h) reveals the different detonation growth behavior between the encased PBXN-110 and LX-17 explosives. Moreover, the detonation rate of the PBXN-110 explosive is higher than that of the LX-17 explosive. Recall that the average detonation rate in the  $x$ -direction is about  $0.752 \text{ cm}/\mu\text{s}$  for the time interval  $t = 10\text{--}15 \mu\text{s}$ .

**4.5. Effect of material models and parameters on the shock-induced detonation.** We have used the shock equation of state (EOS) (4)<sub>1</sub> applicable for most metals, Johnson–Cook plasticity model to describe the high velocity impact response of steel casing and projectile, and the Lee–Tarver ignition and growth model to calculate the reaction rate of the explosive materials. The erosion criterion serves not only as a material failure model, but also to ensure the completion of the analysis. Note that the results we have obtained may depend on the choice of the material models as well as the material parameters. In this section, we delineate the effect of material models and parameters on the shock-induced detonation.

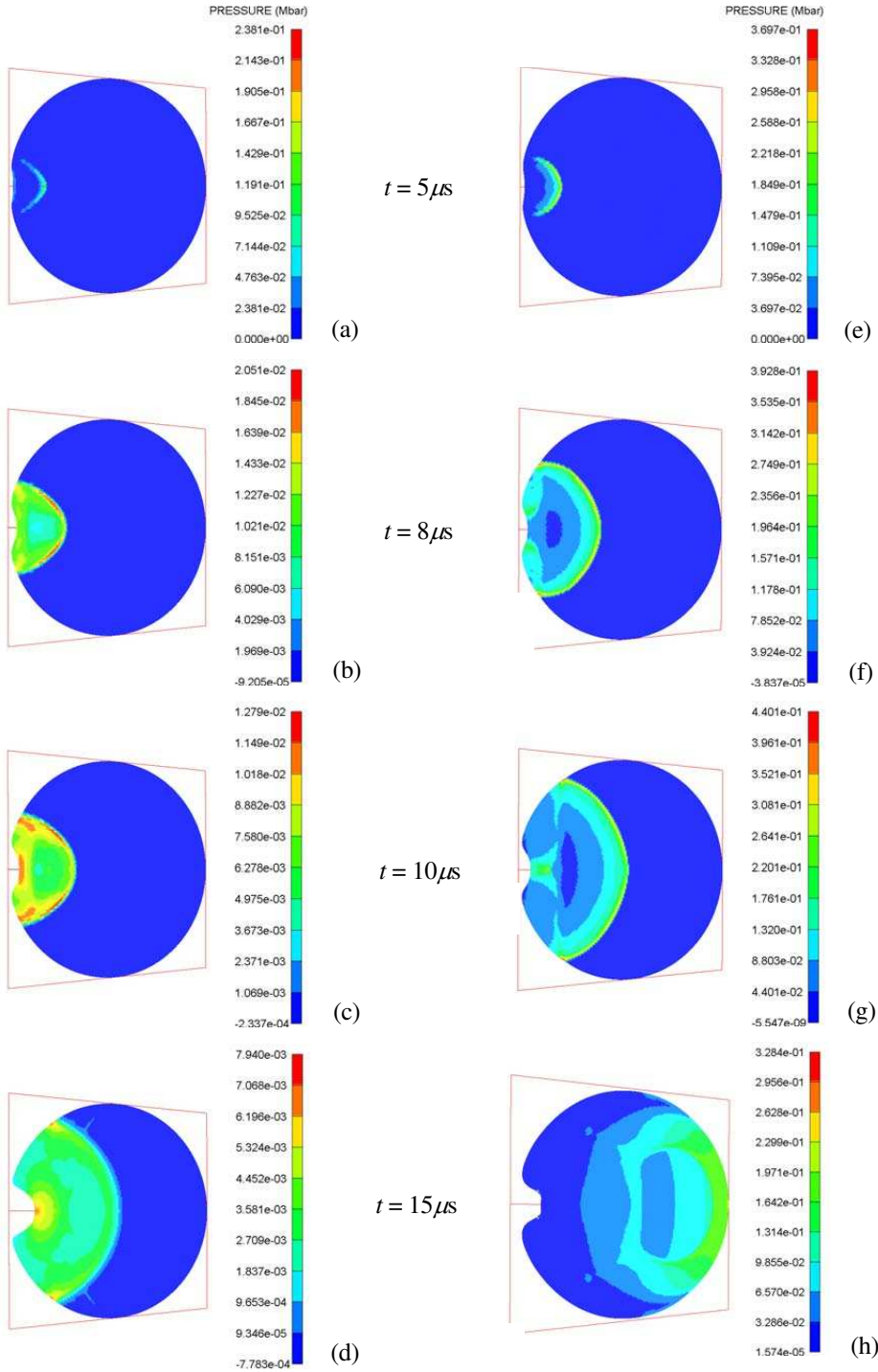


**Figure 12.** Shock wave in circular cross-section at  $z = 0$  of the encased PBXN-110 explosive at  $t = 5 \mu s, 8 \mu s, 10 \mu s$  and  $15 \mu s$ ; (a-d)  $V_p = 2.9$  km/s, (e-h)  $V_p = 3.0$  km/s.

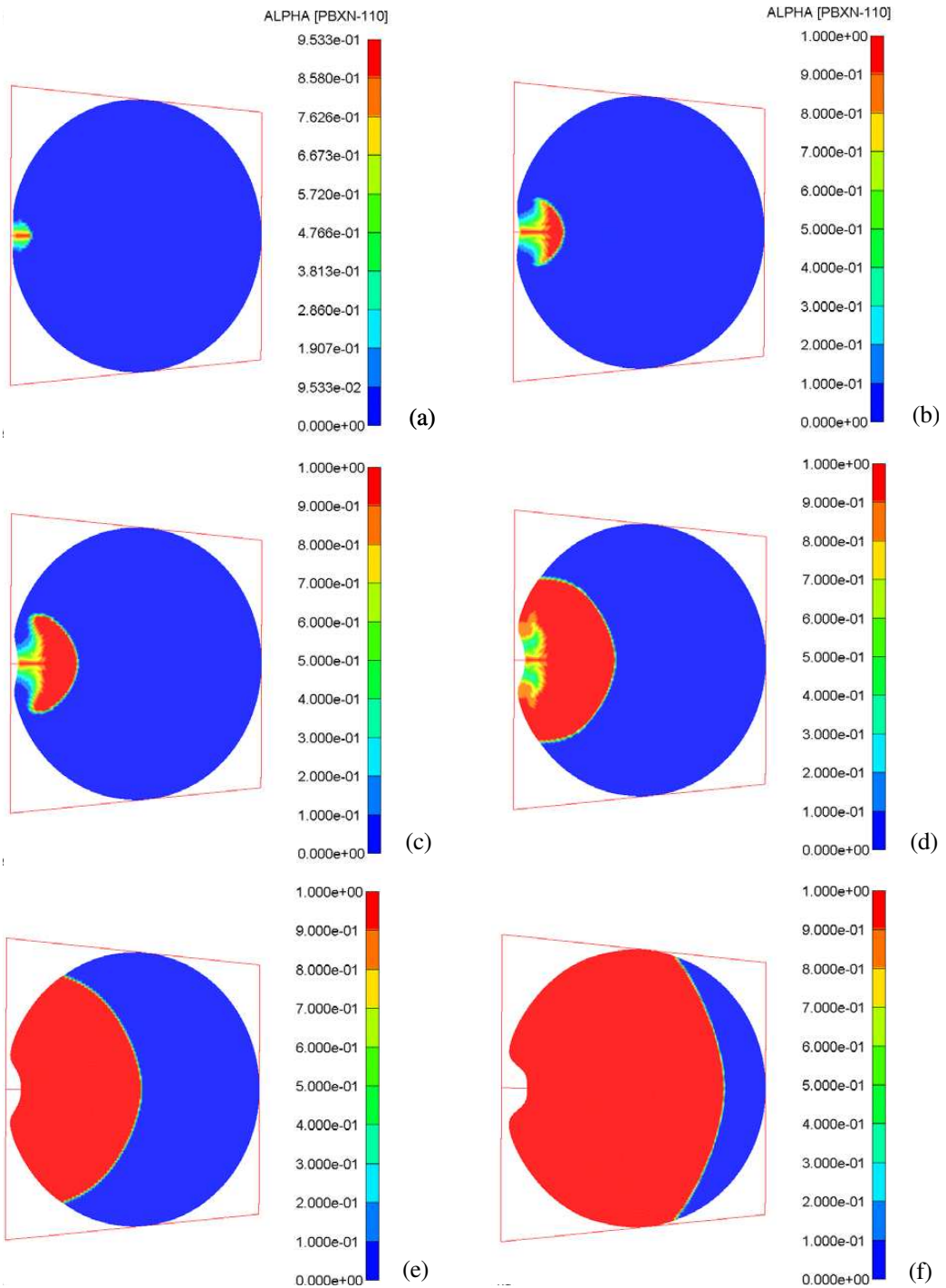


**Figure 13.** Burn fraction in the circular cross-section at  $z = 0$  of the encased PBXN-110 explosive at  $t =$  (a)  $3 \mu\text{s}$ , (b)  $5 \mu\text{s}$ , (c)  $6 \mu\text{s}$ , (d)  $8 \mu\text{s}$ , (e)  $10 \mu\text{s}$ , (f)  $15 \mu\text{s}$  for  $V_p = 3.0 \text{ km/s}$ .

	Cube		Sphere	Plate
	PBXN-110	LX-17		
Shock EOS	3.0 km/s	4.5 km/s	4.8 km/s	1.74 cm × 1.74 cm
Linear EOS	2.8 km/s	3.9 km/s	4.3 km/s	1.64 cm × 1.64 cm

**Table 3.** Comparison of threshold conditions leading to detonation for cases from Sections 4.1–4.4 for steel casing using the shock and linear EOS.

Table 3 compares the threshold values of the projectile velocity or size leading to detonation, calculated with the shock EOS (4)<sub>1</sub> and the linear EOS given by

$$p = K\mu, \tag{5}$$

where  $p$  is the hydrostatic pressure,  $K$  is the material bulk modulus, and  $\mu$  is the material compression defined in Equation (3); for steel considered in this work  $K = 1.59$  Mbar. In every case the threshold value obtained by the linear EOS (5) is lower than that obtained by the shock EOS (4)<sub>1</sub>. For example, the threshold velocity of the cubical projectile calculated with the shock EOS is 4.5 km/sec, while it is 3.9 km/s when the linear EOS is used. This suggests that a proper EOS for the case material and projectiles be used in the simulation of shock-induced detonation of energetic explosives.

In order to delineate the effect of material failure on the shock-induced detonation, we also implement the Johnson–Cook damage model in the steel casing and projectile. The progress of failure is defined by the cumulative damage law  $D = \sum(\Delta\varepsilon/\varepsilon_f)$ , where  $\Delta\varepsilon$  is the increment in effective plastic strain with an increment in loading, and  $\varepsilon_f$  is the failure strain at the current state of the loading which is a function of the mean stress, the effective stress, the strain state and homologous temperature. The expression for the failure strain is given by

$$\varepsilon_f = [D_1 + D_2e^{D_3\sigma^*}][1 + D_4 \log |\dot{\varepsilon}_p^*|][1 + D_5T^*], \tag{6}$$

where  $\sigma'$  is the mean stress normalized by the effective stress,  $D_i$  are material constants whose values are listed in Table 2. Failure is assumed to occur when  $D = 1$ .

Figure 14 depicts the time histories of pressure at points of  $A$  and  $B$  in the encased LX-17 caused by the cubical projectile, computed with (a) the Johnson–Cook damage model only, (b) the erosion criterion only, and (c) both. The numerical calculation without the erosion criterion stops at about  $t = 4.3 \mu s$ . As shown in Figure 14, the time histories of the pressures have no discernible variation among the three cases, other than the fact that no further calculation can be continued for case (a). Further numerical analysis finds that the threshold impact speeds of the projectile obtained with and without the Johnson–Cook damage model are identical, namely, 4.5 km/sec. As far as the threshold condition for shock detonation is concerned, use of the erosion criterion for the failure model for the casing and projectile could be sufficient.

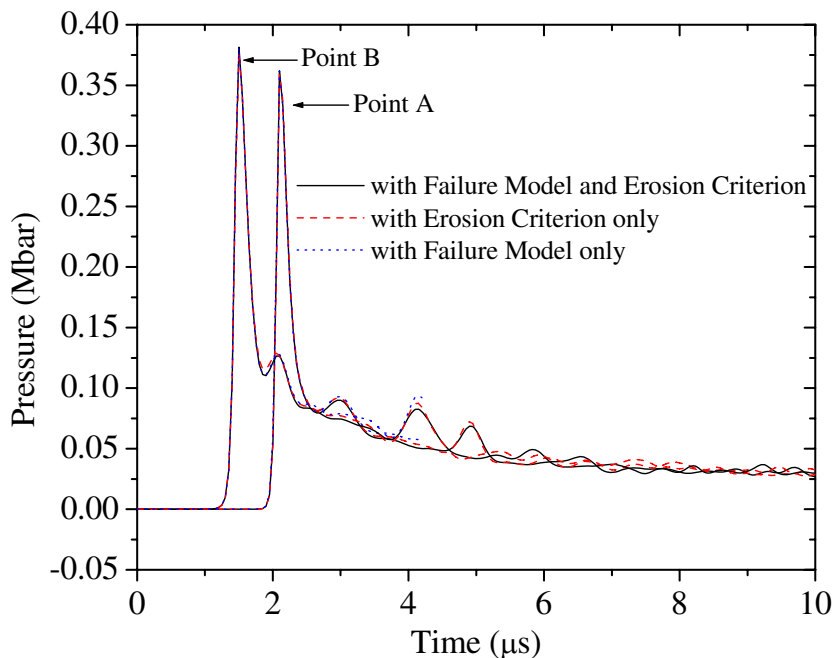


**Figure 14.** Time histories of shock pressure at *A* and *B* in the encased LX-17 explosive for  $V_p = 4.5$  km/s, computed by combining Johnson–Cook damage model and erosion criterion, Johnson–Cook damage model only, and erosion criterion only.

## 5. Summary and conclusions

We have performed a three-dimensional finite element analysis for shock-induced detonation in a mockup consisting of an open-ended steel cylinder filled with LX-17 or PBXN-110 explosive by a normal impact to the cylindrical surface. Three steel projectiles of different shape are examined: (1) a cube of constant mass of 7 g, (2) a sphere of same mass, and (3) a square plate with a constant impact velocity of 2.3 km/s. The thickness of the cube and the flat square projectile is the same. The Lee–Tarver ignition and growth model is employed to describe the reaction rate of the energetic materials. Both the unreacted solid explosive and reacted gaseous product are modeled by the JWL equation of state. The shock equation of state and the Johnson–Cook plasticity model are adopted to describe structural response of the steel casing and projectile. Depending on the projectile investigated, either the threshold detonation velocity or the critical size of the projectile is calculated. The resulting high rate deformation and perforation of the steel cylinder as well as the shock wave and burn fraction in the explosives are presented and discussed.

For the LX-17 explosive encased in the cylinder of 10 cm in length, 0.9525 cm in thickness, and 6.6675 cm in the inner radius, the calculated threshold velocities of the cubical projectile that lead to deflagration and detonation are 3.9 km/s and 4.5 km/s, respectively. The threshold deflagration and detonation velocities are 4.5 km/s and 4.8 km/s for the spherical projectile. The higher threshold detonation velocity for the spherical projectile found here is consistent with those found for the projectiles impacting on a flat surface of a bare, front-covered, or totally confined high explosive. For the square plate projectile

the calculated threshold detonation in-plane dimension is 1.74 cm. For the encased PBXN-110 explosive impacted by the cubical projectile a violent detonation could occur immediately as long as a full reaction in the explosive is initiated in the region near the impact site. The calculated threshold detonation velocity is 3.0 km/s, which is much lower than that for the encased LX-17 explosive. The direct shock-to-detonation transition mechanism simulated is different from the shock-to-deflagration-to-detonation transition found for the LX-17 explosive.

There are some physics missing in the simulations in this work. For instance, cracks in the high explosive may open upon the fragment entering through the container, which may change a slow burn scenario to a full detonation. Further investigations on these issues and detonation tests are suggested.

### Acknowledgements

The authors are grateful to Dr. Jerome Lattery and Dr. Robert Abernathy of New Mexico Institute of Mining and Technology for their valuable discussions for the work. They would also like to thank the reviewers for the valuable comments.

### References

- [Allahdadi et al. 1998] F. A. Allahdadi, D. F. Medina, E. T. Olson, and S. R. Jeffers, "Simulation of impact induced detonation of AIM-120: a novel approach", Technical report AFSC-TR-2000-0002, Air Force Safety Center — Weapons, Space, and Nuclear Safety Division, Kirtland Air Force Base, NM, 1998, Available at <http://handle.dtic.mil/100.2/ADA379702>.
- [Autodyn 2005] Century Dynamic Inc., *AUTODYN Theory Manual*, Century Dynamic Inc., 2005. Revision 4.3.
- [Bahl et al. 1981] K. L. Bahl, H. C. Vantine, and R. C. Weingart, "The shock initiation of bare and covered explosives by projectile impact", pp. 325–335 in *Proceedings Seventh International Symposium on Detonation* (Annapolis, MD), vol. 1, NSWC MP 82-334, Naval Surface Weapons Center, Silver Spring, MD, 16–19 June 1981.
- [Chou et al. 1991] P. C. Chou, D. Liang, and W. J. Flis, "Shock and shear initiation of explosive", *Shock Waves* **1**:4 (1991), 285–292.
- [Cook et al. 1989] M. D. Cook, P. J. Haskins, and H. R. James, "Projectile impact initiation of explosive charges", pp. 1441–1450 in *9th Symposium International on Detonation* (Portland, OR), 27 Aug–1 Sept 1989.
- [Cook et al. 2001] M. D. Cook, P. J. Haskins, R. Briggs, and C. Stennett, "Fragment impact characterization of melt and pbx explosives", pp. 1047–1050 in *Shock compression of condensed matter meeting* (Atlanta, GA), American Institute of Physics, June 24–29 2001.
- [Davison 1997] D. Davison, "Three-dimensional analysis of the explosive initiation threshold for side impact on a shaped charge warhead", Technical report, Shock Transients, Inc., Hopkins, MD, 1997, Available at <http://www.shocktrans.com/DownloadableFiles/STI.InsensitiveMunitions.1997.p%20df>.
- [Forest 1978] C. A. Forest, "Burning and detonation", Technical report LA-7245, Los Alamos Scientific Laboratory, Los Alamos, NM, 1978.
- [Hull et al. 2002] L. M. Hull, J. R. Faulkner, G. T. Gray III, C. M. Caddy, and W. R. Blumenthal, "Initiation experiments on PBXN-110", Technical report LA-UR-02-5024, Los Alamos National Laboratory, Los Alamos, NM, 2002.
- [James et al. 1991] H. R. James, P. J. Haskins, and M. D. Cook, "Effect of case thickness and projectile geometry on the shock initiation threshold for a given explosive", pp. 18:1–15 in *AGARD Conference Proceedings 511* (Neuilly sur Seine, France), NATO Specialists Meeting, 21-23 Oct 1991. p.18/1-15.
- [James et al. 1996] H. R. James, P. J. Haskins, and M. D. Cook, "Prompt shock initiation of cased explosives by projectile impact", *Propell. Explos. Pyrot.* **21**:5 (1996), 251–257.
- [Johnson and Cook 1983] G. R. Johnson and W. H. Cook, "A constitutive model and data for metals subjected to large strains, high strain rates and high temperatures", pp. 541–547 in *Proc. 7th Int Symp Ballistics*, The Hague, The Netherlands, 1983.

- [Johnson and Cook 1985] G. R. Johnson and W. H. Cook, "Fracture characteristics of three metals subjected to various strains, strain rates, temperature and pressures", *Eng. Fract. Mech.* **21**:1 (1985), 31–48.
- [Lattery et al. 2005] J. Lattery, R. Abernathy, and K. Christopherson, "Progress Report", Technical report N60921-93-D-A109, Air Force Safety Center, 2005.
- [Lee and Tarver 1980] E. L. Lee and C. M. Tarver, "Phenomenological model of shock initiation in heterogeneous explosives", *Phys. Fluids* **23**:12 (1980), 2362–2372.
- [Lee et al. 1968] E. L. Lee, H. C. Hornig, and J. W. Kury, "Adiabatic expansion of high explosive detonation products", Technical report UCRL-50422, Lawrence Livermore National Laboratory, Livermore, CA, 1968.
- [Meyers 1994] M. A. Meyers, *Dynamic behavior of materials*, Wiley, New York, 1994.
- [Miller 1996] P. J. Miller, "A simplified method for determining reactive rate parameters for reaction ignition and growth in explosives", Technical report, Naval Air Warfare Center, Weapons Division, China Lake, CA, 1996.
- [Peugeot et al. 1998] F. Peugeot, M. Quidot, and H. N. Presles, "An analytical extension of the critical energy criterion used to predict bare explosive response to jet attack", *Propell. Explos. Pyrot.* **23**:3 (1998), 117–122.
- [Shin and Lee 2003a] H. Shin and W. Lee, "Interactions of impact shock waves in a thin-walled explosive container, I: impact by a flat-ended projectile", *Shock Waves* **39**:4 (2003), 470–478.
- [Shin and Lee 2003b] H. Shin and W. Lee, "Interactions of impact shock waves in a thin-walled explosive container, II: impact by a cone-nosed projectiles", *Shock Waves* **39**:4 (2003), 479–486.
- [Shin and Lee 2003c] H. Shin and W. Lee, "A numerical study on the detonation behavior of double reactive cassettes by impact of projectiles with different nose shapes", *Int. J. Impact Eng.* **28**:4 (2003), 349–362.
- [Starkenberget al. 1984] J. Starkenberg, Y. Huang, and A. Arbuckle, "Numerical modeling of projectile impact shock initiation of bare and covered composition-B, ARBRL-TR-02576", US Army Ballistic Research Laboratory, 1984.
- [Tarver and Hallquist 1981] C. M. Tarver and J. O. Hallquist, "Modeling two-dimensional shock initiation and detonation wave phenomena in PBX 9404 and LX 17", pp. 488–497 in *Proceedings Seventh International Symposium on Detonation* (Annapolis, MD), NSWC MP 82-334, Naval Service Weapons Center, Silver Spring, MD, 1981.

Received 4 Oct 2006. Accepted 26 Feb 2007.

J. K. CHEN: [ChenJnK@missouri.edu](mailto:ChenJnK@missouri.edu)

*Department of Mechanical and Aerospace Engineering, University of Missouri, Columbia, Missouri, United States*

HSU-KUANG CHING: [hching@vt.edu](mailto:hching@vt.edu)

*Department of Mechanical and Aerospace Engineering, University of Missouri, Columbia, Missouri, United States*

FIROOZ A. ALLAHDADI: [Firooz.Allahdadi@kirtland.af.mil](mailto:Firooz.Allahdadi@kirtland.af.mil)

*Air Force Safety Center, Kirtland AFB, New Mexico, United States*

